Wnt signaling modulates tissue mechanics, actin order, and regeneration in *Hydra vulgaris*

Thomas Perros[1], Stéphane Joly[1], Adama Mbaye[1], Philippe Marcq[2], Olivier Cochet-Escartin[1,*].

1 : Université Claude Bernard Lyon 1, CNRS, Institut Lumière Matière, Villeurbanne, France.

2 : Physique et Mécanique des Milieux Hétérogènes, PMMH, CNRS, ESPCI Paris, Université PSL, Sorbonne Université, Université Paris Cité, F-75005, Paris, France

* : correspondence should be addressed to olivier.cochet-escartin@univ-lyon1.fr

Abstract

Hydra vulgaris is a powerful model organism in the study of axial patterning and regeneration. While recent models emphasize the importance of mechanical cues in establishing body axis symmetry in *Hydra* tissue spheres, the precise role of the Wnt pathway, known to be central to axial patterning, in regulating tissue mechanics and cytoskeletal organization remains unclear. In this paper, we pharmacologically modulated the canonical Wnt pathway using Alsterpaullone and iCRT14 and assessed their effects on regeneration, tissue rheology, and actin organization in *Hydra* tissue spheres. We found that Wnt activation prevents full regeneration, softens the constitutive tissues, disrupts osmotic oscillations, leads to an accumulation of dense actin filaments but impairs their orientational order. Conversely, we found that Wnt inhibition partially impairs regeneration and reduces actin filament presence while preserving alignment. Using micro-aspiration and time-lapse imaging, we characterized the changes in the nonlinear elasticity and osmotic oscillations under both conditions. These results support and unify two existing mechano-chemical models of *Hydra* patterning, suggesting that Wnt-driven feedbacks on both tissue stiffness and actin order contribute to the robust emergence of body axes. Our findings highlight the possibility of redundant mechanisms in the *Hydra* patterning system, potentially explaining its robustness.

Key words

Hydra regeneration, Wnt signaling, actin nematic order, tissue rheology, mechano-chemical patterning, morphogenesis.

Introduction

Hydra vulgaris is a freshwater cnidarian well-known for its ability for whole body regeneration. Any piece of excised tissue, as well as cellular reaggregates can spontaneously reform a full, viable organism in just a few days (1). As such, it has long served as a model organism to study biological patterning and morphogenesis from theoretical and experimental perspectives. With their simple body plan, *Hydra* offers a unique system to study how an organizing axis can arise spontaneously in the absence of external cues. Following the seminal works of Alan Turing on reaction-diffusion systems (2) or of Lewis Wolpert on the French flag model (3), this question was first tackled from a purely biochemical point of view. Gierer and Meinhardt proposed in the 1970s a reaction-diffusion model inspired by Turing's work and adapted to the specific case of *Hydra* (4). This model recapitulated regeneration and grafting experiments through the interplay of two morphogens, a head activator and a head inhibitor. Further, the canonical Wnt pathway in general, and the ligand HyWnt3 in particular were shown to have all the expected properties of the head activator in this model. Not only is this pathway self-activating (5), it was also shown that the Wnt/β-catenin pathway controlled the formation of a head organizer (6, 7). Decades of research, however, have failed to uncover an equivalent of the head inhibitor in the Gierer Meinhardt model. Some candidates were identified such as Sp5 (8), Dkk1/2/4 (9), or *Hydra* astacin-7 (10). However, none of them have proven to be fully satisfactory for this role, as each showed characteristics that were inconsistent with the predictions of the model. While this did not constitute definitive proof, it suggested that the model remained incomplete.

In recent years, the focus in the field has switched to a mechano-chemical view of *Hydra* regeneration. Key to this change was the observation that osmotically driven mechanical oscillations seemed required for axis definition (11). During their regeneration, excised tissue pieces and cellular re-aggregates start by forming a so-called tissue sphere in which the two main epithelial monolayers, the endoderm and ectoderm, form a spherical lumen. The osmolarity of the inner medium being higher than that of the outside medium, water is actively pumped to the inside of the lumen which starts swelling. It does so to the point where mechanical tension in the tissue becomes too large and the tissues rupture and the lumen quickly deflates. The resulting wound is then healed, and a new cycle begins, leading to a succession of saw-tooth like oscillations. At some point these oscillations show a reduction in amplitude and period, indicative of the formation of a new functional mouth (12) and this has been referred to as a switch from Phase I to Phase II oscillations (11). This showed that the head organizer must be defined prior to this shift in osmotic oscillations. More intriguing was the fact that when these oscillations were blocked by increasing the osmolarity of the outside medium, regeneration failed. Tissue spheres would remain alive but would never show signs of elongation in one direction and no apparition of tentacles (11, 13). This was a clear indication that the apparition of the head organizer is, at least partly, mechanically regulated and linked to tissue stretch, tension or rupture. This was later confirmed by molecular analysis which showed a direct feedback loop through which tissue stretch induces the expression of HyWnt3 and other Wnt ligands (13).

In parallel, other researchers have put forward the idea that the organization of supracellular actin filaments, called myonemes, in the ectoderm could be linked to axis definition (14). In the adult *Hydra*, these myonemes align with the organizing axis all over the body column. In an excised tissue piece, this organization can be partially inherited despite the folding back into a spherical shape. This organization seemed to correlate strongly with the axis of the regenerated animal with nematic defects in the organization co-localizing with the future mouth and foot

(15). This suggested that spontaneous pattern formation might not be necessary in *Hydra* regeneration from excised tissue pieces. It didn't explain, however, how patterning is achieved in cellular aggregates which lack any inherited myonemes or why osmotic oscillations would be necessary in the regenerative process.

Nevertheless, both approaches shared an emphasis on mechanical cues in *Hydra* patterning and, to help resolve this question, we recently proposed a mechanical characterization of regenerating *Hydra* tissue spheres using parallelized micro-aspiration experiments (16). We showed that, during osmotic oscillations, they behave as non-linear elastic spherical shells whose mechanical properties were quantified. Based on these different results, two new mechano-chemical models of *Hydra* patterning have emerged in the past year, focusing on different ingredients.

The first model builds upon the results of (14, 15) and highlights the role of actin nematic order in the ectoderm (17). The topology of tissue spheres requires that two +1 nematic defects are formed. At these locations, the myonemes meet in an aster-like configuration. Because of acto-myosin contractility, these defects turn into regions of high tensile stresses and thus high cellular deformations. The model supposes that this local strain triggers a mechano-genetic feedback loop leading to a local activation of the Wnt signaling pathway. To ensure the stabilization of this proto-organizer, the model also hypothesizes that the actin organization responds to a putative Wnt gradient by aligning along its direction, finishing to establish a full nematic order. The fact that an interplay between a morphogen gradient and a nematic field can stabilize nematic defects and drive patterning has been demonstrated theoretically (18), further supporting the rationale of this model. However, in addition to two strong hypotheses, this model requires the pre-existence of a partial actin nematic order and thus is not sufficient to explain patterning in regeneration from cellular aggregates where this order is completely lost. It also doesn't require the existence of osmotic oscillations since cellular deformations result from the contractility of the actin network and not the swelling of the tissue spheres.

The second model focuses on osmotic oscillations and the same hypothesis of a strain-dependent morphogen source (19). By random fluctuations of either deformations or mechanical properties, swelling of the tissue spheres creates a region with slightly larger deformations. In turn, this region starts expressing more of the morphogen. The authors showed that Wnt activation could make the tissue more deformable. Mechanical deformations could thus be locally amplified by a positive feedback loop. In addition, as one region becomes softer and highly deformed, the rest of the tissue sphere is less deformed, limiting the expression of the morphogen. This model thus resembles a classic reaction-diffusion process with a major difference: the long-range inhibitor is not of a chemical nature but of a mechanical one. As this model does not require any pre-existing actin organization, it could apply for both excised tissue pieces and cellular aggregates. However, it relies on hypotheses and does not require any specific actin nematic order.

To shed light on these apparent contradictions, one needs to test the underlying hypotheses of both models. On the one hand, the effect of tissue deformations on Wnt activation are well established. On the other, the effects of Wnt activation on rheology and actin organization remain poorly understood. A difficulty in achieving this goal is that, under normal conditions, Wnt activation on *Hydra* tissue spheres is highly localized and difficult to observe *in vivo*. To overcome this limitation, we decided to work on tissue spheres on which the Wnt pathway was either activated or inhibited everywhere.

The aim of this paper is thus to modulate Wnt activation and quantify the response of entire *Hydra* tissue spheres in terms of regeneration, rheology and actin nematic order. To achieve this, we used two drugs, alsterpaullone and iCRT14, which were previously used in *Hydra* to demonstrate the involvement of the canonical Wnt pathway in axis definition (6, 20–24).

We achieved Wnt pathway activation by treating the animals with alsterpaullone (AP). It was previously demonstrated that treating full *Hydras* with AP induces the formation of ectopic tentacles along the body column (6). AP is a kinase inhibitor that specifically targets GSK3 (25). From a molecular biology perspective, GSK3 is a kinase that phosphorylates β-catenin. This phosphorylation inhibits β-catenin's proliferation. When the Wnt pathway is activated, phosphorylation is blocked, allowing β-catenin to accumulate, translocate to the nucleus, and express target genes. AP therefore blocks this phosphorylation and forces the activation of the Wnt pathway even in the absence of ligands. A common protocol, described in (26), involves immersing full *Hydras* in $5\mu M$ AP for $48h$, followed by transferring them back to normal conditions. Two to three days after the end of the treatment, the *Hydra* were puffy, with numerous small tentacles sprouting from their bodies. AP treatment gave head-like characteristics to the body column, including strong expression of both head organizer and head inhibitory signals (6). This explains the emergence of multiples tentacles spots without the formation of complete heads.

On the opposite, inhibition of the Wnt pathway was achieved by treating *Hydras* with iCRT14. It has been demonstrated (27) that this molecule specifically interferes between β-catenin and the transcription factor TCF4, thereby inhibiting the transcription of target genes in the Wnt pathway. Previous works have shown that by inhibiting this signaling pathway, iCRT14 blocked *Hydra* regeneration after amputation (22, 23). Indeed, $72h$ after bisection, *Hydras* treated with this drug, although they had closed the wound, exhibited a rounded oral end without any tentacle or hypostome formation (22). The same observation was made for the foot, where after $48h$, no cell differentiation had occurred (22).

In this paper, we treated full *Hydras* with AP or iCRT14 before excising tissue spheres which had a uniform high- or low-level activation of the Wnt pathway. Then, using large scale screening and timelapse imaging, our previously published microaspiration setup, transgenic *Hydra* lines and 3d spinning disk microscopy, we were able to quantify the effect of these two drugs on regeneration at the organism scale, tissue rheology, osmotic oscillations and actin nematic order. Overall, our results strongly support the hypotheses of the two recent models of *Hydra* patterning. AP prevented full regeneration, induced clear defects in both patterning and morphogenesis which we explain by a softening of the tissues as well as a misalignment of myonemes. iCRT14, on the other hand, only partially blocked regeneration, showed no significant effect on tissue stiffness but induced a disassembly of actin filament. As a result, we argue in the Discussion section that the two current models are not contradictory and should be merged. Having two different mechanisms for axial patterning should add robustness to the system. We finally propose that such robustness could be key in explaining the great plasticity of *Hydra* regeneration.

Methods

Hydra care and lines used

Hydras were kept in a suitable environment called *Hydra* medium (HM) which consists of pure water (filtered with Direct-Q 3UV, Merck, Frankfurt, Germany), $0.5mM\ N_aHCO_3$, $1mM\ C_aCl_2$, $0.1mM\ MgCl_2$, $0.08mM\ MgSO_4$ and $0.03mM\ KnO_3$ at a pH between 7 and 7.3 adjusted using HCl. The cultures were stored in Tupperware containers, which were then kept in an incubator (Pol-Ekko-Aparature, Wodzislaw Slaski, Poland) in the dark at a fixed temperature of 18°C. The *Hydras* were fed twice a week with newly hatched *Artemia* (Hobby; Dohse Aquaristik, Grafschaft, Germany). Four *Hydra vulgaris* lines were maintained and used for experiments: a wild type (AEP) line and transgenic strains. A watermelon (WM) and a reverse watermelon (RWM) line expressing GFP in the ectoderm (for WM)/endoderm (RWM) and DsRed2 in the ectoderm (WM)/endoderm(RWM) (28), both under the control of an active actin promoter and an ectoderm LifeAct-GFP line (29).

Preparation of tissue spheres and pharmacological treatments

Tissue spheres were made by hand-cutting slices of tissue from the body column, using a sterile scalpel (Bistouri UU no. 10, Holtex, Aix-en-Provence, France). First, the head and foot were removed via two transverse cuts. Then, we cut 3-4 slices from the remaining body column. This resulted in ring-shaped pieces. These were then cut in half to form strips which we left to close into a sphere for 3 to 4 hours. These cuts were made until 6 to 8 pieces were obtained from a single *Hydra*. To improve their precision, these manipulations were carried out under an illuminated stereomicroscope (Leica Microsystems, Wetzlar, Germany).

For Wnt modulation, we prepared solutions of $5\mu M$ AP with 0.025% DMSO (Sigma-Aldrich, St Louis, USA) or $5\mu M$ iCRT14 (Sigma-Aldrich) with 0.05% DMSO in HM. These solutions were prepared from stock solutions at $4000X$ (100% DMSO) for AP and $2000X$ (100% DMSO) for iCRT14. Parental animals were pre-incubated in the respective drugs in HM for 2h (iCRT14) or 48h (Alsterpaullone) prior to excision. Tissue fragments were excised and incubated in the same drug-containing HM during folding into tissue spheres and the subsequent experiments.

Young's modulus measurements

All micro-aspiration experiments were carried out as previously described in (16). For each batch of six tissue spheres, the samples were inserted in the microfluidic channel at t_0. We then applied a series of steps of applied pressures. This was achieved by varying the height of an open syringe using hydrostatic pressure. Images of the aspirated samples were acquired on a Leica DMi6 inverted fluorescence microscope equipped with a 10x objective. For each pressure step, we measured the length L of tissue inside the holes. We then computed the real aspirated length as:

$$\delta z = L - (R_0 - \sqrt{R_0^2 - R_p^2})$$

Where R_0 is the radius of the tissue sphere and R_p the radius of the hole, here 50µm. We then performed, in Python, linear fits of the obtained stress-strain curves (Figure 2 (b)) and extracted a measure of the Young's modulus E using Equation 1 and $h_0 = 20\mu m$, $\nu = 0.495$ and $C_S = 23.4$. Numerical simulations shown in Supplementary Figure 2 were also performed as described in (16) using Comsol Multiphysics (COMSOL Inc, Burlington, USA).

Analysis of osmotic oscillations

For imaging, Watermelon (WM) strain tissue spheres were individually placed in custom agarose wells. A 2% agarose (Carl Roth, Karlsruhe, Germany) solution in HM was poured into a well of a 6-well plate (Thermo Fisher Scientific, Waltham, Massachusetts) to form a uniform layer approximately 5mm thick. After gel solidification, cylindrical holes of were punched into the agarose, using a 1mm Harris Uni-Core puncher (Sigma-Aldrich), to create individual imaging chambers. Each well was then filled with HM and covered with a thin layer of paraffin oil (VWR, Radnor, USA) to prevent evaporation. For experiments requiring both agarose wells and the application of AP or ICRT14 on *Hydra* tissue spheres, the drugs were added to the medium and to the HM used to make the gel to prevent dilution effects. Time-lapse imaging was carried out over a continuous period of 24 h, with images acquired every 15 min on a Leica DMi6 inverted fluorescence microscope equipped with a 10x objective.

Image sequences from the GFP channel were batch processed using ImageJ. Initial segmentation was performed via Li's thresholding method, followed by morphological operations: hole filling, erosion (to separate adjacent particles), and dilation (to recover eroded areas). Only regions with an area exceeding 10 000µm^2 and circularity greater than 0.30 were retained for analysis. A custom-made macro automated this workflow. Assuming radial symmetry, sphere area A was converted to radius R using: $R = \sqrt{\frac{A}{\pi}}$. Phase I oscillations were identified manually based on amplitude and periodicity. A Python script normalized radii to the minimum radius within each tracked series and detected peaks using the find_peaks function. For each oscillation, the following parameters were computed: duration (time between successive minima), maximal radius (peak value), and swelling rate (slope of a linear regression between the first minimum and the maximum radius). All oscillatory metrics were averaged per sphere for statistical comparisons.

Quantification of regeneration

For each experiment, a total of 30 tissue spheres were prepared and kept in custom made wells in 2% agarose in six well plates. They were imaged under a MZ16 stereomicroscope (Leica Microsystems) with an automated Tango stage (Marzhauser, Wetzlar, Germany) for six days after t_0. From the resulting timelapses, we manually noted the time of their death or of the first tentacle apparition.

For circularity measurements, we used both the RWM and LifeAct lines and acquired images under an epifluorescence DMI6 microscope (Leica Microsystems) equipped with a 10x objective. The resulting images were binarized in ImageJ (NIH, Bethesda, USA) and the projected area A and perimeter P of the sample was extracted. Circularity, C, was then computed as

$$C = 4\pi \frac{A}{P^2}$$

Observation of actin nematic order

We used LifeAct-ectoderm GFP tissue spheres and full *Hydras*. Images were acquired as zstacks under an Eclipse Ti2 microscope (Nikon Europe, Amstelveen, Netherlans) equipped with a CSU-W1 spinning disk unit (Yokogawa, Tokyo, Japan) and an Orca Fusion BT camera (Hamamatsu, Shizuoka, Japan). Optical planes were acquired every 2µm and maximum intensity projections

were generated in ImageJ. For tissue spheres, the areas with visible myonemes were manually drawn, the outline of each sample was automatically segmented in ImageJ. We then computed the ratio of the surface covered by myonemes to the total surface on the sample and classified the results in four different classes based on that ratio.

Statistical analysis

All plots were designed in Python. In Figures 1, 2 and 3, the box plots represent the median and the quartiles of the corresponding distributions. Individual measurements are also shown as black dots. Statistical tests were performed for each pair of conditions using a two-sample Student's t-test. We assumed statistical relevance if the p-value of this test was lower than 1% and this was represented as stars on the corresponding plots.

Results

Experimental approach

To study the effect of perturbing the canonical Wnt pathway on *Hydra* regeneration, we focused on *Hydra* tissue spheres excised from organisms either untreated or pre-incubated with 5 μM alsterpaullone for 48h or 5μM iCRT14 for 2h. The concentrations and timing of exposure were taken from the literature and have been shown to have clear effects both at the molecular level (6, 23) and in terms of regeneration (20, 22, 30, 31). After excision, samples were kept exposed to the drugs to ensure their effect would be maintained during further experiments. They were left to fold back into tissue spheres for three hours at which point the experiments were started at a time we refer to as t_0.

Effect of Wnt modulation on *Hydra* regeneration

The first effect of Wnt modulation we decided to study was on the outcome of regeneration. We followed tissue spheres for six days after excision and, each day, we counted how many were dead, how many still resembled tissue spheres and how many were regenerated. Of note, to avoid biases, we counted a sample as regenerated as soon as it showed at least one tentacle, in line with previous works (13). As expected, we found that a vast majority (around 90%) of untreated samples properly regenerated and did so within a typical time of 2-4 days (Figure 1(a)). In stark contrast, samples treated with AP all died within the time scale of the experiment, most of them between days 2 and 4. This is different from Wnt-overexpressing *Hydras* (5) which are viable, suggesting that AP has a lethal effect different from its role as a Wnt activator.

iCRT14 treatments showed a mixed effect. Lethality was high, around 50%, but the remaining half of the samples still managed to regrow at least one tentacle. Given the well-established role of the Wnt canonical pathway in defining the head organizer in *Hydra* this result might seem counterintuitive. It is however in line with (22) which showed that, at a similar concentration, regeneration after bisection was not fully blocked and that some samples still managed to regenerate either the head or foot. Only higher concentrations fully blocked regeneration. In addition, we did observe a delay in regeneration with no sample showing tentacles after 2 days, compared to roughly 40% for untreated samples. Overall, despite the high degree of lethality we observed, we argue that 5μM iCRT14 remains the best compromise for experimental investigations, leaving enough samples to study while showing a clear phenotypical effect.

Although AP induced an important lethality, we still observed an effect on morphogenesis during the first 24h of the experiments. Control samples, as expected, started spherical and gradually acquired an elongated, ellipsoid shape (Figure 1(b)). In contrast, AP-treated samples deviated from a spherical shape at t_0, showing bulges that became more pronounced over time (Figure 1(b)). After 24h, they often showed multiple bulges and seemed swollen (Figure 1(b)). To quantify this effect, we measured the circularity of the samples at t_0 and t_0+24h in all three conditions. The circularity *C*, sometimes called roundness, of a two-dimensional figure measures its deviation from a circle (for which C=1). It remains high for ellipses and falls as the figure becomes more tortuous. We indeed found that at t_0, the circularity of AP-treated samples was significantly lower than that of control and iCRT14-treated samples (Figure 1(c)). 24h later, the mean circularity had decreased for all conditions but remained lower for AP-treated samples (Figure 1(c)) than for the others. This suggests an important role of Wnt signaling in *Hydra* not only for patterning but also for morphogenesis.

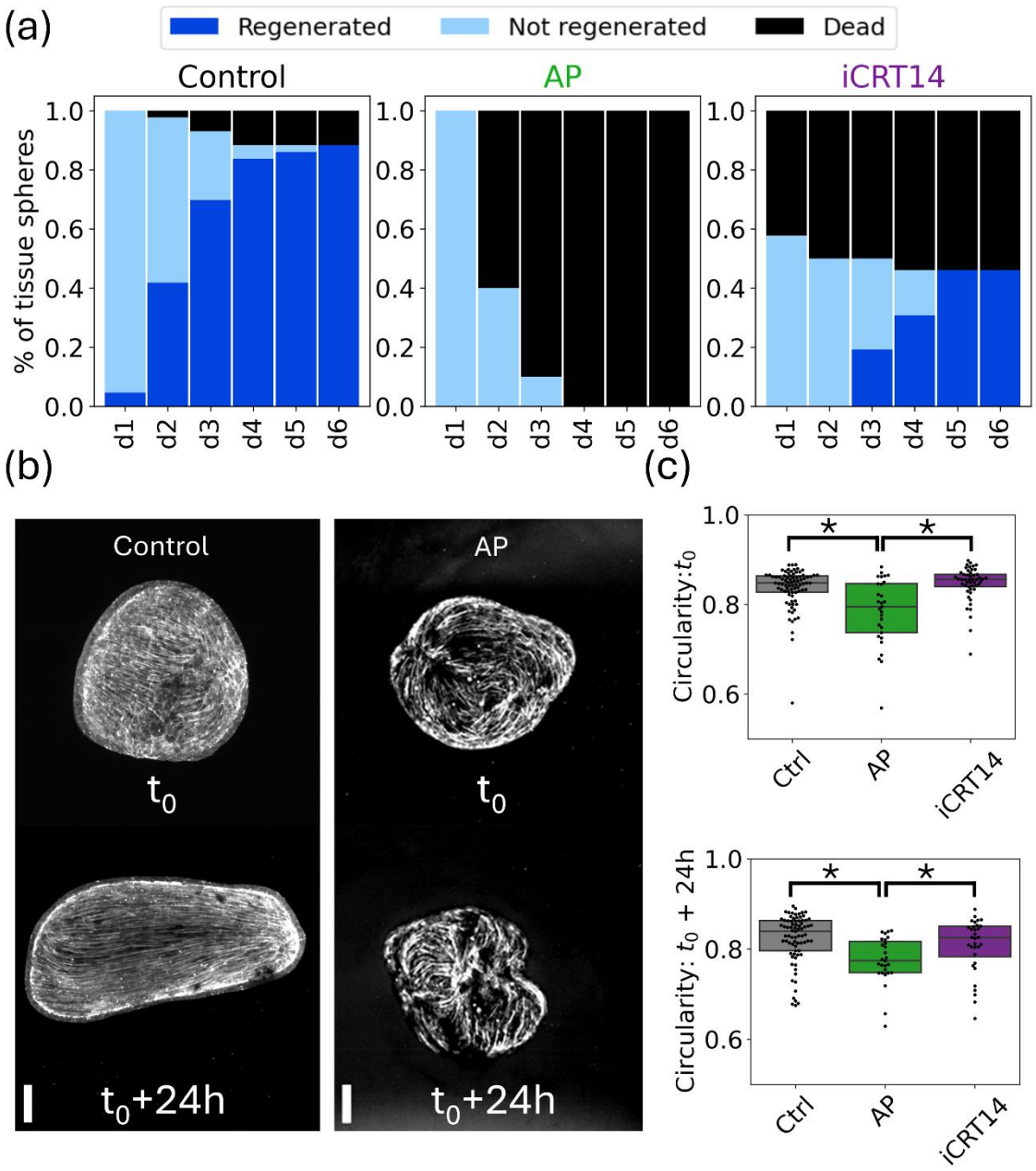

Figure 1. Effect of Wnt modulation on regeneration and morphogenesis. (a) Fraction of regenerated (dark blue), unregenerated (light blue) and dead (black) Hydra tissue spheres from day 1 (d1) to day 6 (d6) after t_0. Data is shown for controls on the left, AP-treated samples in the center and iCRT-treated samples on the right, n= 43,30 and 26, respectively. (b) Maximum intensity projections of LifeAct-GFP tissue spheres in control (left) and AP-treated samples (right) at t_0 and t_0+24h, scale bars: 100 microns. (c) Quantification of circularity for all three treatments at t_0 (n=82,29 and 49 in the order shown on the plot) and t_0+24h (n=77,27 and 32). The boxes display the median and quartile of each distribution and stars represent statistical significance with a p-value<0.01.

These results show that the experimental conditions we selected from the literature were indeed relevant. Although the drugs had a significant lethality at the studied doses, most samples were still viable after a day, giving us ample time to perform further experiments. More importantly, both drugs had clear effects either on regeneration time or on the morphology of the samples. Finally, the swollen aspects of AP-treated tissue spheres suggested changes in their mechanical properties which we decided to investigate next.

Wnt activation softens *Hydra* tissue spheres

As described in the introduction, a recent model of *Hydra* patterning relies on the idea that Wnt activation could induce an increase in tissue deformability (19). The authors tested this hypothesis using a Wnt-overexpressing *Hydra* line and measured surface tensions using micro-aspiration. Recently, we performed a thorough mechanical characterization of regenerating tissue spheres insisting on the importance of the non-linear elastic properties of these samples (16) and their behavior as 3d elastic shells rather than 2d surfaces. We therefore decided to repeat this characterization under both AP and iCRT14 treatments.

Experimentally, we used a custom-made microfluidic device (Supplementary Figure 1) allowing to perform six micro-aspirations in parallel (Figure 2(a)) (16, 32). Theoretically, we used the Saint-Vernan Kirchhoff model and finite element simulations to show that in a certain applied pressure range (400 Pa – 4kPa), the length of aspirated tissue δz increases linearly with the applied pressure ΔP and that the Young's modulus E of the sample can be extracted using the following relationship (16):

$$\Delta P = C_s \frac{2Eh_0}{(1-\nu)R_0^2}\delta z + \Delta P_0 \qquad (1)$$

Where $C_s = 23.4$ is a dimensionless pre-factor, ν is the Poisson coefficient, h_0 and R_0 are its thickness and radius, respectively, and ΔP_0 is a negative intercept, signature of the non-linear elastic behavior at low applied pressures (16).

When we applied the same approach to AP and iCRT treated samples, we first observed that the linear relationship between applied pressure and aspirated length still held (Figure 2(b)). Using Equation 1, we then extracted measurements of E for each sample based on the slope of the linear relationship and a precise measurement of R_0 . Doing so, we found that AP significantly decreased the elastic modulus of *Hydra* tissue spheres (Figure 2(c)) from (4.4 ± 3.3).10^2 Pa for control samples to (2.9 ± 1.7).10^2 Pa. On the other hand, we found no difference between controls and iCRT14-treated samples (Figure 2(d)) which had an elastic modulus of (4.2 ± 2.2).10^2 Pa.

We then decided to better characterize these changes in mechanical properties by focusing on low applied pressures which had not be explored in our previous work. We turned to a range of

applied pressures between 50 and 1500 Pa and we observed a non-linear relationship between the aspirated length and the applied pressure. This offered a direct observation of a stress stiffening effect in *Hydra* tissue spheres. Of note, the AP-induced difference in stiffness was also clearly visible in this pressure range. For a given applied pressure, AP-treated samples were significantly more deformed than control ones (Figure 2(d)).

We also checked whether our previous choice of the Saint-Venan Kirchhoff model to describe *Hydra* tissue spheres was relevant in that small deformation regime. Since there is no analytical expression relating δz and ΔP in the geometry of micropipette aspiration, we reverted to numerical simulations. Using a finite element framework, we simulated the aspiration of an elastic spherical shell with parameters matching those of the experiments. By trial and error, we modified the elastic modulus of the shell until we managed to reproduce measurements made on a single sample. We found very good agreement for a value of $E = 750Pa$ (Supplementary Figure 2), validating the use of this specific rheological model to describe *Hydra* tissue spheres.

Overall, these results strongly support the hypothesis of (19), namely that Wnt activation increases deformability, in our interpretation lowering stiffness. Although our experiments were performed on homogenous tissue spheres where Wnt was either activated or inhibited everywhere, it is reasonable to imagine that a local activation of the Wnt pathway, as it occurs in normal regeneration, would lead to a local reduction in elastic modulus. Then, under an isotropic influx of water due to osmotic differences, it is expected that a spherical shell of anisotropic stiffness will deform more where it is softer and less where it is stiffer, providing a clear mechanical basis for the strain localization at the heart of the model of (19). On the other hand, the lack of impact of iCRT14 was to be expected. Inhibition of Wnt activation should only induce small, local differences with control samples on which Wnt activation is localized. Therefore, iCRT14-treated samples should be mechanically very similar to untreated ones. Finally, our data clearly demonstrate the non-linear nature of the elastic response of *Hydra* tissue spheres (Figure 2(d)) which was only indirectly observed in (16). We argue that this nonlinear elastic response could be important in *Hydra* patterning.

A natural consequence of these changes in mechanical properties is the effect they might have on the osmotic oscillations observed during *Hydra* regeneration which are known to play an important role in patterning (11, 13).

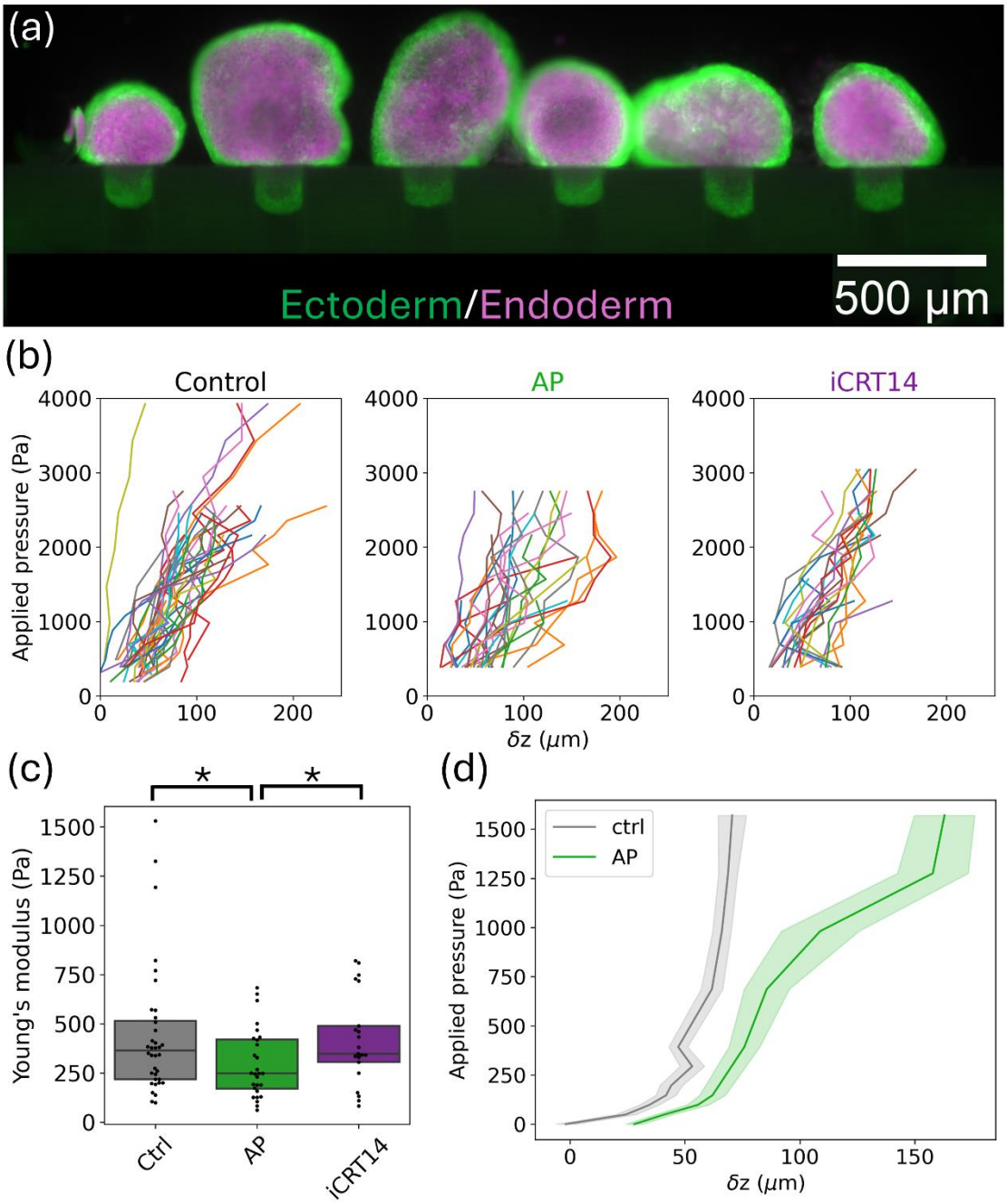

Figure 2. (a) Snapshot of six Hydra tissue spheres aspirated within the microfluidic device. (b) Plots of applied pressure versus aspirated length δz for controls on the left, AP-treated samples in the center and iCRT-treated samples on the right. Each colored line corresponds to a single sample, n= 36,28 and 21, respectively. (c) Distribution of Young's moduli extracted from each sample from (b) using linear fit and Equation 1. The boxes display the median and quartile of each distribution and stars represent statistical significance with a p-value<0.01.(d) Averaged responses of control (grey) and AP-treated samples (green) at low applied pressures. The lines represent the average and the shaded area the standard error of the mean, n=22 and 27.

Effect of Wnt modulation on osmotic oscillations

To characterize osmotic oscillations, we used a transgenic *Hydra* line expressing GFP in the ectoderm (28) and time-lapse fluorescent microscopy to extract a mean radius over time from

395 an automated segmentation of the outline of the sample (Figure 3(a)). We then decided to focus
396 on the so-called Phase I oscillations which are the relevant ones for *Hydra* patterning (11, 12).
397 We manually selected these specific oscillations as the earliest, longest and with the largest
398 amplitude and identifying the switch to Phase II oscillations. In line with the results of (19), we
399 observed a potential difference for AP-treated samples which seemed to display oscillations of
400 higher amplitude and longer duration (Figure 3(b)). To confirm this observation and obtain better
401 statistics, we placed, at t_0, up to thirty tissue spheres in individual microwells made in agarose
402 gels, acquired high resolution time lapses for each of them and extracted their radius over time
403 $R(t)$. To characterize these oscillations, we focused on four parameters (Supplementary Figure
404 3).

405 First, the swelling rate $\dot{R}(t) = \frac{dR(t)}{dt}$ is the average speed at which the samples swell. Previous
406 work has shown that this swelling rate increases proportionally with the rest radius R_0 of the
407 tissues spheres (11) and we therefore report the relative swelling rate: $\frac{\dot{R}(t)}{R_0}$. We did not find any
408 differences in the relative swelling rate between control, AP-treated and iCRT14-treated
409 samples. Since this swelling is known to be due to osmotic differences between the inside and
410 outside medium of the tissue spheres, we thus conclude that modulation of the Wnt pathway
411 does not change either the osmolarity of the inner medium or the water permeability of the
412 tissue spheres.

413 Second, the stretch ratio $\alpha(t) = \frac{R(t)}{R_0}$ is a measure related to the mechanical strain ε of the
414 spheres through $\varepsilon = \alpha - 1$. An important measurement is the maximum stretch ratio, α_{max}, at
415 which the tissue spheres rupture. Indeed, since tissue rupture is due to a failure of cell-cell
416 adhesions (16), it is thought to occur at a certain critical stress. The stresses experienced by the
417 tissue increasing with both the strain and the stiffness of the tissue, a decrease in stiffness is
418 expected to lead to an increase in the maximum stretch ratio. This is what we observed, with AP-
419 treated samples showing a significant increase in α_{max}, from 1.31 ± 0.07 for controls to 1.56 ±
420 0.20 for AP-treated samples (Figure 3(d)). Of note, this corresponded to a roughly two-fold
421 increase in the maximum mechanical strain ε_{max} which was good agreement with the observed
422 changes in Young's modulus between these two conditions. Finally, as expected, we did not find
423 any significant difference in α_{max} for iCRT-treated samples for which α_{max} was 1.33 ± 0.09
424 (Figure 3(d)).

425 Third, we measured the average duration of osmotic oscillations in each condition. Since we
426 showed the relative swelling rate to be constant, we expected the average duration of
427 oscillations to directly correlate with α_{max}. We found the average durations to be 3.60 ± 0.98h,
428 7.94 ± 3.86h and 4.10 ± 1.57h for controls, AP-treated and iCRT-treated samples, respectively
429 (Figure 3(e)).

430 Finally, we counted the number of Phase I oscillations before the switch to Phase II. In (13), the
431 authors proposed that the key parameter controlling pattern formation and the switch to Phase II
432 oscillations is the overall amount of tissue stretching, akin to the area under the curve of the
433 radius overt time. If so, AP-treated samples should display fewer oscillations since each of these
434 would be longer and larger. We were able to confirm this as we observed a significant decrease
435 in the number of oscillations for AP-treated samples but not for iCRT14-treated ones (Figure
436 3(f)).

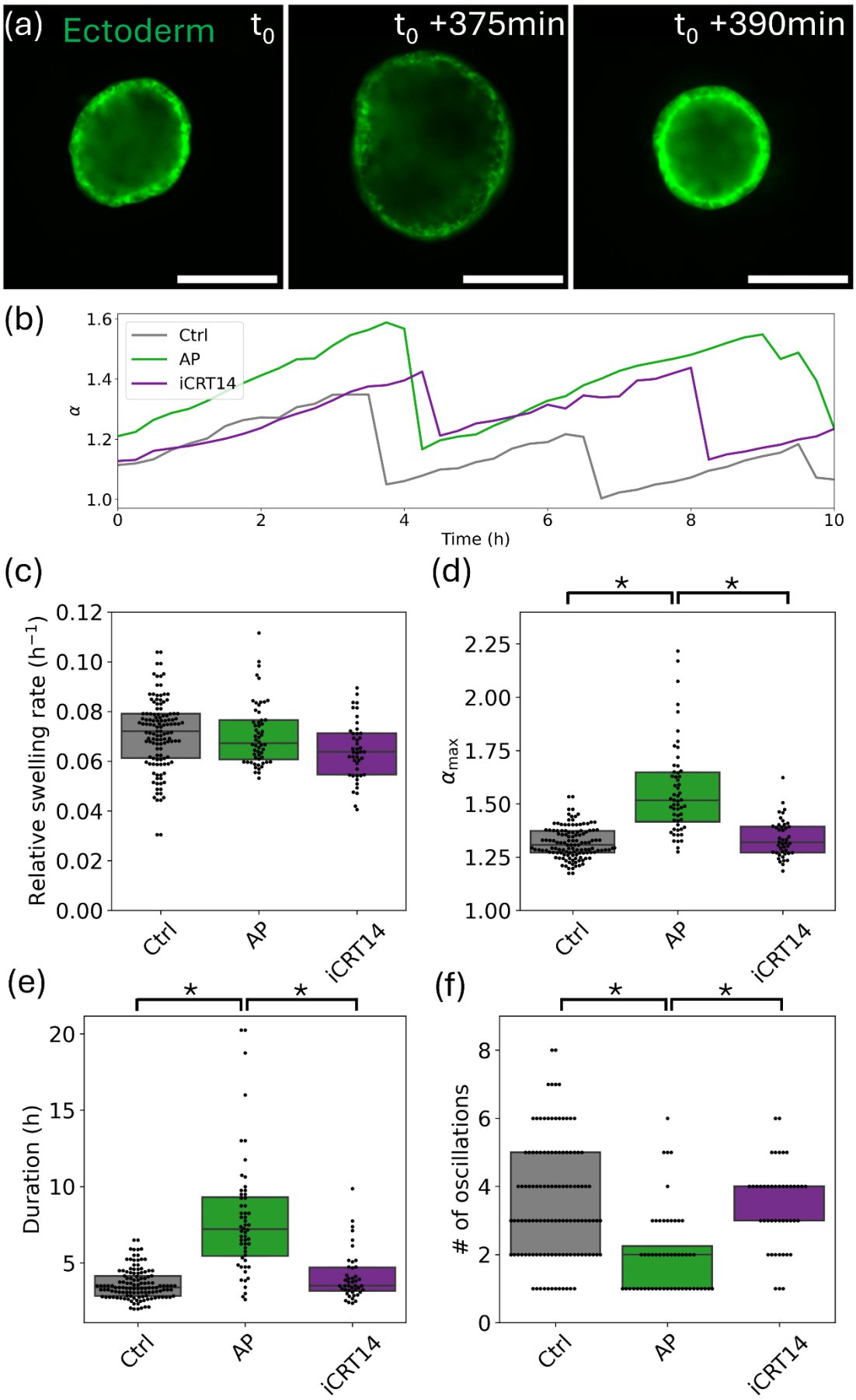
(a)
Ectoderm
t_0
t_0 +375min
t_0 +390min
(b)
Ctrl
AP
iCRT14
α
Time (h)
(c)
Relative swelling rate (h^{-1})
Ctrl
AP
iCRT14
(d)
α_{max}
(e)
Duration (h)
(f)
# of oscillations

Figure 3. (a) Snapshot of a Hydra tissue sphere with fluorescence in the ectoderm at three different time points. These images are used to extract the area and then the radius of the tissue sphere. Scale bars: 250 microns. (b) Examples of the dynamics of $\alpha(t) = \frac{R(t)}{R_0}$ in the three different conditions, controls in grey, AP in green and iCRT in purple. (c-f) quantification of all four parameters characterizing osmotic oscillations: relative swelling rate in (c), maximum stretch ratio in (d), duration of oscillations in (e) and number of oscillations in (f). In each, boxes display the median and quartile of each distribution and stars represent statistical significance with a p-value<0.01. n=126,56 and 44, respectively.

All these results are a clear confirmation of a softening of the tissue spheres when the canonical Wnt pathway is activated. The applied drugs, on the other hand, had no effect on the swelling rates, indicating that swelling is fully controlled by osmotic fluxes and not mechanical properties. These results are also similar to those of (19) which were obtained with a Wnt3-overexpressing line rather than through AP treatment. The observed trends are indeed the same but the exact values obtained for α_{max} and the average duration of the oscillations are slightly different. These differences could be explained by different effects of the genetic and pharmacological manipulations, larger groups in our work or differences in the detection of Phase I oscillations.

Effect on actin nematics

The last key ingredient in *Hydra* patterning we investigated was the organization of ectodermal myonemes. To do so, we used a transgenic *Hydra* line expressing LifeAct-GFP in the ectoderm. This line allows an observation of both cortical actin, outlining the shape of the cells, and the myonemes. We used 3d spinning-disk microscopy and maximum intensity projections to achieve high spatial resolution. We observed effects of our treatments on both the amount of cortical actin and the level of alignment of myonemes. For control samples, we confirmed that both were observable but that myonemes only covered a fraction of the samples. As explained in (14), this partial actin nematic order is inherited from the parent *Hydra*. We decided to quantify the amount of myonemes by measuring the fraction of the projected area of the samples they covered (Supplementary Figure 4). We classified each sample into one of four categories depending on this fraction, whether it was between 0-10%, 10-50%, 50-90% or over 90%. For controls, the samples were fairly well distributed between the first three classes (Figure 4(a)). Importantly, the observable myonemes were clearly aligned along a single direction (Figure 4(b)) defining the future oral-aboral axis.

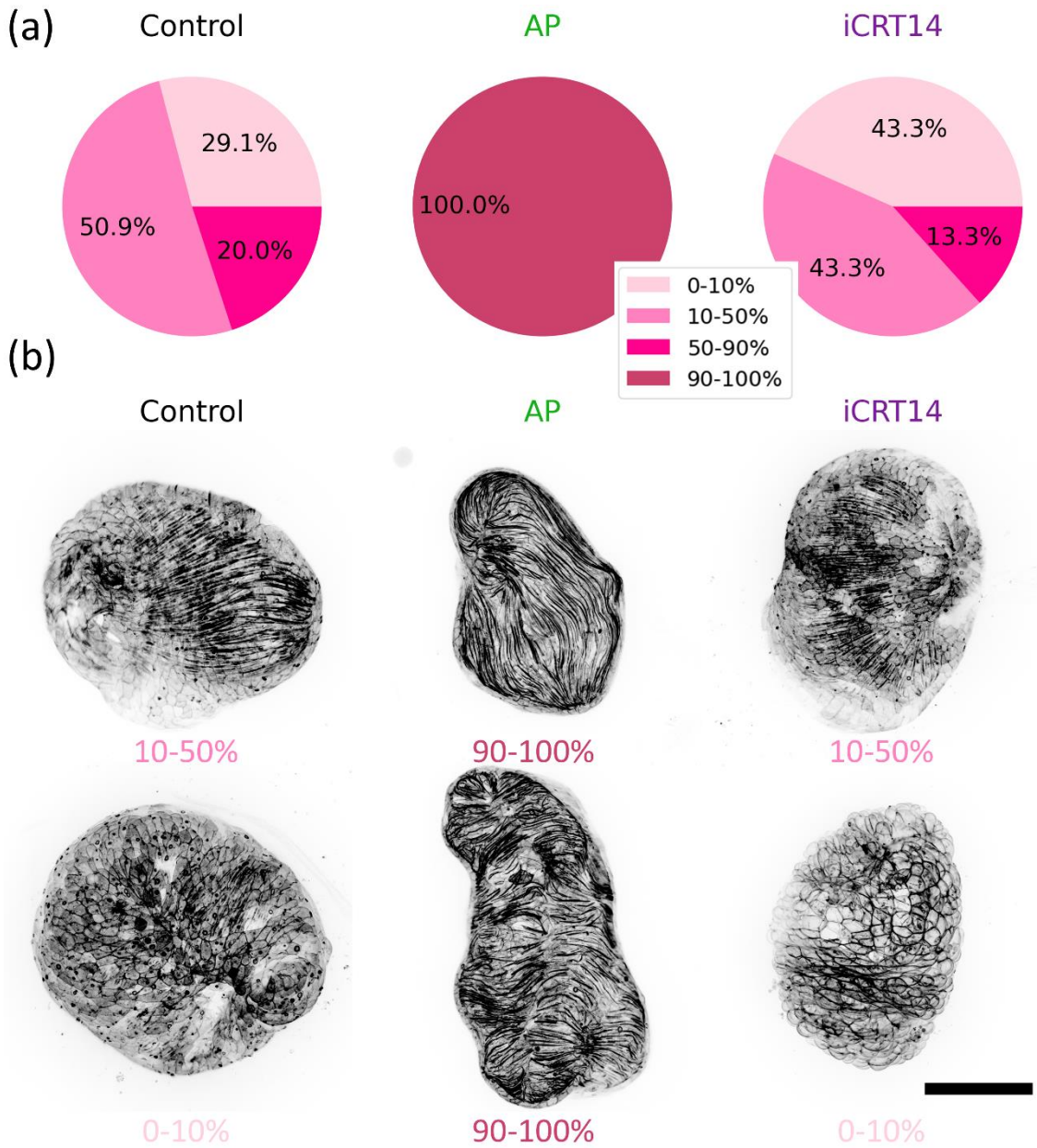

Figure 4. (a) Distribution of samples depending on the fraction of their surfaces covered by visible myonemes. The four categories: 0-10%, 10-50%, 50-90% and 90-100% are shown in shades of pink. Distributions are shown for all three conditions, controls on the left, AP-treated samples in the center and iCRT-treated samples on the right. n=55,22 and 30, respectively. (b) Two examples of maximum intensity projections of LifeAct-GFP Hydra tissue pieces in each condition shown in each column. Scale bar: 100 microns.

Our observations were slightly different for iCRT-treated samples. We observed a significant reduction in the amount of observable myonemes, the 0-10% class being more represented under this perturbation (Figure 4(a)) while the 10-50% and 50-90% were less populated. Still, the few remaining myonemes showed a partial nematic order with a single axis of alignment (Figure 4(b)). This was a first indication that inhibiting the canonical Wnt pathway led to a slow disassembly of surpacellular actin structures without perturbing their directional alignment.

The situation was strikingly different for AP-treated samples. First, on n=36 samples, we never observed any sign of cortical actin, only the myonemes were visible. Image acquisition was done

in the same way and with the exact same parameters suggesting that it was a real decrease in cortical actin rather than an effect of much brighter myonemes hiding the signal from cortical actin. Indeed, all samples were fully covered in myonemes and fell into the 90-100% class (Figure 4(a)) suggesting a higher level of organization. Their alignment, however, was clearly perturbed and they appeared much wigglier and randomly aligned (Figure 4(b)). More examples of all three conditions can be found in Supplementary Figure 5.

Since myoneme organization is inherited, we then asked what the effect of Wnt modulation on the ectodermal myonemes of full *Hydras* was. As expected, controls showed a full coverage of myonemes and a perfect alignment in the oral-aboral axis (Supplementary Figure 6). For AP-treated full *Hydra*, we observed an altered organization. The filaments were wavy and curved (Supplementary Figure 6). The shape of the *Hydras* seemed to follow this trend, being abnormally arched. The organization of fibers in iCRT14-treated whole *Hydra* was preserved and still showed a clear alignment along the head-tail axis $24h$ after immersion in the drug. However, we observed in many *Hydras* the appearance of a 'cluster' effect in the organization of cortical actin. The cell actin cortex became particularly visible in certain regions of the animal while myonemes were no longer visible in these regions.

Overall, these observations were similar to those in tissue spheres, and both can be summarized as follows: iCRT14 induces the disassembly of myonemes which still maintain their alignment when they are visible; AP stabilizes and enhances the formation of myonemes but disrupts their alignment which becomes multidirectional and seems to reduce the amount of cortical actin. This is in strong support of the hypothesis of (17) that actin nematic order aligns with gradients of Wnt activation. In the absence of Wnt activation, these myonemes slowly disappear whereas under strong, homogenous activation, they are numerous but do not align. Importantly, the decrease in signal from cortical actin in AP-treated samples is a potential explanation for the observed softening of the whole tissue. Tissue elasticity in epithelia is known to depend both on cell-cell adhesions and single cell mechanical properties especially their cortical tension (33). A decrease in this tension is a strong candidate to explain the observed softening of tissue spheres under Wnt activation.

Discussion

In this work, we used pharmacological means to modulate the activation of the Wnt pathway in a model organism for regeneration and axial patterning. By making the molecular landscape of *Hydra* tissue spheres homogenous, this approach allowed us to directly test different couplings between Wnt signalling and key ingredients in patterning: osmotic oscillations, rheology, actin nematic order. In addition, we tested the effect of these drugs on the outcome of regeneration which, to our knowledge, had not been systematically assessed in this context.

Doing so, we observed and better characterized the non-linear elastic behavior of *Hydra* tissue spheres (Figure 2(d)). Of note, we showed that their elastic behavior held up to deformations as large as 30-40% before rupturing. This is uncommon but was observed for suspended MDCK monolayers (34) which also displayed a non-linear elastic rheology. In this system, the maximum deformations were even as large as 60%. Although *Hydra* tissue spheres are composed of two epithelial layers stuck together by extra-cellular matrix, their similarity with flat, suspended monolayers suggest that their elastic rheology might be a common signature of epithelia. How these biological systems can sustain such large deformations in an elastic

530 regime remains unanswered and their response to deformations at the cellular scale should be
531 investigated to better understand this ability.

532 Furthermore, we demonstrated that activation of the Wnt pathway has a direct impact on
533 elasticity, making the tissues softer. Wnt, through the canonical and non-canonical pathways,
534 has a wide array of effects at the cellular and tissular level linked to mechanical properties. For
535 example, activation of the canonical pathway was shown to destabilize adherens junctions in
536 cancer cell lines (35). One key mechanism is the recruitment of β-catenin from cadherin-based
537 cell-cell junctions to the cytoplasm and nucleus, increasing the amount of free β-catenin and
538 down-regulating genes involved in these junctions (36). Another effect of this pathway is to
539 induce the endocytosis of focal adhesions (37). Since these adhesions couple the cytoskeleton
540 to the extra-cellular matrix, their endocytosis reduces the cell-matrix adhesion. These effects
541 are not limited to the canonical Wnt pathway. For example, activation of the Wnt-PCP pathway in
542 *Xenopus* embryos impacts the fibronectin matrix, Rac signaling and tissue tension (38). Which
543 molecular and cellular mechanisms are involved in the observed softening of *Hydra* tissue
544 spheres under Wnt activation is a question naturally occurring from our work.

545 We argue that this feedback between Wnt and elasticity has a particular significance in *Hydra*.
546 Wnt activation has always been thought of as a patterning mechanism in this organism. The
547 apparition of a local hotspot of Wnt activation is seen as the first step of axis definition. While
548 this remains true, our results suggest that this patterning by Wnt also induces heterogeneities in
549 mechanical properties. Such heterogeneities are known to be critical for morphogenesis: the
550 development of the proper shape of organisms (39). Morphogenesis results from the interplay
551 between the mechanical properties of the tissues and the forces acting on them. In other
552 systems, it has been shown that both force and stiffness heterogeneities can lead to axis
553 elongation (40, 41). They can direct both the direction of elongation and its dynamics. In the
554 case of *Hydra*, the main driving force is osmotic swelling which is homogenous. Since
555 mechanical properties are now thought to correlate with Wnt activity, one expects elongation of
556 the samples in the direction of the Wnt hotspot. Therefore, the formation of this Wnt hotspot
557 would be key both in the formation of the head organizer and in the morphogenetic event of axis
558 elongation. This is further supported by our observation that AP induces defects in
559 morphogenesis with the apparition of multiple bulges on regenerating tissue spheres (Figure
560 1(b-c)). Having molecular patterning and axis elongation controlled by a single system could
561 provide plasticity which is a signature property of *Hydra* regeneration which can succeed from a
562 variety of initial conditions.

563 A consequence of these changes in mechanical properties is the changes we observed in
564 osmotic oscillations. Many biological structures share the lumen-like structure of *Hydra* tissue
565 spheres: cysts in general which are a common motif in the brain, the heart, the gut etc, and
566 blastocysts in particular... It has been shown in blastocysts that hydraulic oscillations, similar to
567 osmotic oscillations in *Hydra*, play a role in controlling embryo size and stem cell fate (42).
568 Theoretical work even proposes a framework explaining how these oscillations can regulate the
569 size of growing luminal structures (43). This process could thus be quite general and applicable
570 to a large variety of structures. Our results could provide a benchmark against which to test
571 models further, offering perturbed conditions where both the oscillations and the outcome of
572 morphogenesis are impaired in a quantifiable way.

573 Another important finding of our work is the effect of Wnt modulation on actin organization. We
574 found two major effects. First, Wnt activity seemed to correlate with the number of visible
575 myonemes: the more Wnt activity, the more myonemes. Second, homogenous Wnt activation

seemed to modify the alignment of these actin fibers. They were aligned in a single direction in control conditions and along multiple directions under AP treatment. These results are similar to some obtained in mammary epithelial cells. Using soluble Wnt3a proteins, the authors showed a stabilization and enhanced directional alignment of actin fibers (44). Similarly, (45) showed on hematopoietic stem cells that the Wnt ligand Wnt5a induces actin polymerization, increasing the amount of filamentous actin through a regulation of ROCK. Although the precise mechanisms at play in *Hydra* are still unknown, it has already been shown theoretically that actin alignment along a morphogen gradient could explain not only axial patterning but also budding , tentacle formation and the structure of the mouth (18). A coupling between nematic fields and diffusing chemical signals might thus offer a new, important class of patterning mechanisms which should be further studied both experimentally and theoretically. The ubiquity of the Wnt pathway in development and axis definition and its potential effects on both tissue rheology and actin organization strongly suggest its importance in the morphogenesis of many different organisms.

Finally, in the specific context of *Hydra* regeneration, our results should help settle ongoing debates. As described previously, the current state of the art proposes two different models, one focusing on actin nematic order (17) and the other on osmotic oscillations, changes in rheology and mechanically induced Wnt activation (19). Interestingly, our work supports the hypotheses underlying both models. We therefore propose that they are not mutually exclusive and should, instead, be combined. Such a combination could be summarized as follows: either by random local fluctuations in mechanical properties, the existence of a partial actin nematic order or both, some regions of a regenerating tissue sphere will experience larger deformations. Because of the non-linear elasticity, such small fluctuations in deformations could be leveraged into larger fluctuations in stresses (16). These areas would then start expressing more Wnt ligands in accordance with (13). Based on our observations, Wnt activation would have a dual effet: a local softening of the tissue and a recruitment and alignment of myonemes. Softening would further localize deformations in these areas under the isotropic swelling due to the osmotic flux. If a +1 nematic defect pre-existed in that region, it would be stabilized, if not, it would form. As demonstrated in (15), such a +1 defect in a contractile network would further localize deformations and end up at the position of the head organizer. We propose that such a mechanism would add redundancy to the patterning system and answer existing questions in the field.

Indeed, one main weakness of the model focusing on actin nematic was to explain how patterning occurred in cellular re-aggregates which do not inherit any myonemes. Notably, a recent study demonstrated that molecular axial patterning preceded the emergence of a fully organized actin network (46). We argue that, in this situation, axial patterning is mainly driven by osmotic oscillations and a feedback loop between tissue deformations, Wnt activation and tissue softening. On the other hand, it was long thought that blocking osmotic oscillations by adding sucrose to the outer medium led to a complete inhibition of regeneration, all tissue spheres failing to break symmetry and define a new axis. Recent data has shown that although samples in isotonic conditions fail to regenerate, they still elongate along the axis of alignment of myonemes (17). In that situation, patterning and morphogenesis could be driven solely by acto-myosin contractility and tissue softening at the location of nematic defects driven by Wnt activation, even in the absence of osmotic oscillations. Further theoretical and numerical work will be needed to confront such a model with all existing experimental observations. For instance, it would be valuable to test the outcome of the regeneration of cellular aggregates in the absence of osmotic oscillations, a situation in which both drivers of patterning would be

absent. Still, the idea of a redundant system which could drive both patterning, and morphogenesis remains very exciting to understand the remarkable robustness and plasticity of *Hydra* regeneration.

Conclusion

In this study, we pharmacologically modulated the canonical Wnt pathway in *Hydra* tissue spheres to investigate its impact on regeneration, tissue mechanics, and actin organization. We show that Wnt activation leads to tissue softening, disrupted actin alignment, altered osmotic oscillations, and impaired regeneration. Conversely, Wnt inhibition reduces actin filament density while preserving mechanical properties and partial regenerative capacity. These findings demonstrate that Wnt signaling affects not only axial patterning but also the mechanical and structural properties of regenerating tissues.

Ackowledgments

This work was partially funded by the Mission pour les Initiatives Transverses et Interdisciplinaires of CNRS (Project MeChemReg to OCE and PM).

References

1. Gierer, A., S. Berking, H. Bode, C.N. David, K. Flick, G. Hansmann, H. Schaller, and E. Trenkner. 1972. Regeneration of hydra from reaggregated cells. *Nat. New Biol.* 239:98–101.

2. Turing, A.M. 1952. The Chemical Basis of Morphogenesis. *Philos. Trans. R. Soc. B Biol. Sci.* 237:37–72.

3. Wolpert, L. 1969. Positional information and the spatial pattern of cellular differentiation. *J. Theor. Biol.* 25:1–47.

4. Gierer, A., and H. Meinhardt. 1972. A theory of biological pattern formation. *Kybernetik*. 12:30–9.

5. Nakamura, Y., C.D. Tsiairis, S. Özbek, and T.W. Holstein. 2011. Autoregulatory and repressive inputs localize Hydra Wnt3 to the head organizer. *Proc. Natl. Acad. Sci. U. S. A.* 108:9137–42.

6. Broun, M., L. Gee, B. Reinhardt, and H.R. Bode. 2005. Formation of the head organizer in hydra involves the canonical Wnt pathway. *Development*. 132.

7. Hobmayer, B., F. Rentzsch, K. Kuhn, C.M. Happel, C.C. von Laue, P. Snyder, U. Rothbächer, and T.W. Holstein. 2000. WNT signalling molecules act in axis formation in the diploblastic metazoan Hydra. *Nature*. 407:186–189.

8. Vogg, M.C., L. Beccari, L. Iglesias Ollé, C. Rampon, S. Vriz, C. Perruchoud, Y. Wenger, and B. Galliot. 2019. An evolutionarily-conserved Wnt3/β-catenin/Sp5 feedback loop restricts head organizer activity in Hydra. *Nat. Commun.* 10:312.

9. Augustin, R., A. Franke, K. Khalturin, R. Kiko, S. Siebert, G. Hemmrich, and T.C.G. Bosch. 2006. Dickkopf related genes are components of the positional value gradient in Hydra. *Dev. Biol.* 296:62–70.

10. Ziegler, B., I. Yiallouros, B. Trageser, S. Kumar, M. Mercker, S. Kling, M. Fath, U. Warnken,

M. Schnölzer, T.W. Holstein, M. Hartl, A. Marciniak-Czochra, J. Stetefeld, W. Stöcker, and S. Özbek. 2021. The Wnt-specific astacin proteinase HAS-7 restricts head organizer formation in Hydra. *BMC Biol.* 19:1–22.

11. Kücken, M., J. Soriano, P.A. Pullarkat, A. Ott, and E.M. Nicola. 2008. An osmoregulatory basis for shape oscillations in regenerating hydra. *Biophys. J.* 95:978–85.

12. Wang, R., T. Goel, K. Khazoyan, Z. Sabry, H.J. Quan, P.H. Diamond, and E.-M.S. Collins. 2019. Mouth Function Determines the Shape Oscillation Pattern in Regenerating Hydra Tissue Spheres. *Biophys. J.* 117:1145–1155.

13. Ferenc, J., P. Papasaikas, J. Ferralli, Y. Nakamura, S. Smallwood, and C.D. Tsiairis. 2021. Mechanical oscillations orchestrate axial patterning through Wnt activation in Hydra. *Sci. Adv.* 7.

14. Livshits, A., L. Shani-Zerbib, Y. Maroudas-Sacks, E. Braun, and K. Keren. 2017. Structural Inheritance of the Actin Cytoskeletal Organization Determines the Body Axis in Regenerating Hydra. *Cell Rep.* 18:1410–1421.

15. Maroudas-Sacks, Y., L. Garion, L. Shani-Zerbib, A. Livshits, E. Braun, and K. Keren. 2020. Topological defects in the nematic order of actin fibres as organization centres of Hydra morphogenesis. *Nat. Phys.* 1–9.

16. Perros, T., A. Biquet-Bisquert, Z. Ben Meriem, M. Delarue, P. Joseph, P. Marcq, and O. Cochet-Escartin. 2024. Mechanical characterization of regenerating Hydra tissue spheres. *Biophys. J.* 123:1792–1803.

17. Maroudas-Sacks, Y., S. Suganthan, L. Garion, Y. Ascoli-Abbina, A. Westfried, N. Dori, I. Pasvinter, M. Popović, and K. Keren. 2025. Mechanical strain focusing at topological defect sites in regenerating Hydra. *Dev.* 152.

18. Wang, Z., M.C. Marchetti, and F. Brauns. 2023. Patterning of morphogenetic anisotropy fields. *Proc. Natl. Acad. Sci. U. S. A.* 120:e2220167120.

19. Weevers, S.L., A.D. Falconer, M. Mercker, H. Sadeghi, D. Rozema, J. Ferenc, J.-L. Maître, A. Ott, D.B. Oelz, A. Marciniak-Czochra, and C.D. Tsiairis. 2025. Mechanochemical patterning localizes the organizer of a luminal epithelium. *Sci. Adv.* 11:2286.

20. Gee, L., J. Hartig, L. Law, J. Wittlieb, K. Khalturin, T.C.G. Bosch, and H.R. Bode. 2010. β-catenin plays a central role in setting up the head organizer in hydra. *Dev. Biol.* 340:116–124.

21. Reddy, P.C., A. Gungi, S. Ubhe, S.J. Pradhan, A. Kolte, and S. Galande. 2019. Molecular signature of an ancient organizer regulated by Wnt/β-catenin signalling during primary body axis patterning in Hydra. *Commun. Biol. 2019 21*. 2:1–11.

22. Gufler, S., B. Artes, H. Bielen, I. Krainer, M.K. Eder, J. Falschlunger, A. Bollmann, T. Ostermann, T. Valovka, M. Hartl, K. Bister, U. Technau, and B. Hobmayer. 2018. β-Catenin acts in a position-independent regeneration response in the simple eumetazoan Hydra. *Dev. Biol.* 433:310–323.

23. Cazet, J., A. Cho, and C. Juliano. 2021. Generic injuries are sufficient to induce ectopic Wnt organizers in Hydra. *Elife*. 10:e60562.

24. Steichele, M., L. Sauermann, Q. Pan, J. Moneer, A. de la Porte, M. Heß, M. Mercker, C. Strube, H. Flaswinkel, M. Jenewein, and A. Böttger. 2025. Notch signaling mediates between two pattern-forming processes during head regeneration in Hydra. *Life Sci.*

Alliance. 8.

25. Leost, M., C. Schultz, A. Link, Y.Z. Wu, J. Biernat, E.M. Mandelkow, J.A. Bibb, G.L. Snyder, P. Greengard, D.W. Zaharevitz, R. Gussio, A.M. Senderowicz, E.A. Sausville, C. Kunick, and L. Meijer. 2000. Paullones are potent inhibitors of glycogen synthase kinase-3β and cyclin-dependent kinase 5/p25. *Eur. J. Biochem.* 267:5983–5994.

26. Reinhardt, B., M. Broun, I.L. Blitz, and H.R. Bode. 2004. HyBMP5-8b, a BMP5-8 orthologue, acts during axial patterning and tentacle formation in hydra. *Dev. Biol.* 267:43–59.

27. Gonsalves, F.C., K. Klein, B.B. Carson, S. Katz, L.A. Ekas, S. Evans, R. Nagourney, T. Cardozo, A.M.C. Brown, and R. Das Gupta. 2011. An RNAi-based chemical genetic screen identifies three small-molecule inhibitors of the Wnt/wingless signaling pathway. *Proc. Natl. Acad. Sci. U. S. A.* 108:5954–5963.

28. Glauber, K.M., C.E. Dana, S.S. Park, D.A. Colby, Y. Noro, T. Fujisawa, A. Richard Chamberlin, and R.E. Steele. 2013. A small molecule screen identifies a novel compound that induces a homeotic transformation in Hydra. *Dev.* 140:4788–4796.

29. Aufschnaiter, R., R. Wedlich-Söldner, X. Zhang, and B. Hobmayer. 2017. Apical and basal epitheliomuscular F-actin dynamics during Hydra bud evagination. *Biol. Open*. 6:1137–1148.

30. Reinhardt, B., M. Broun, I.L. Blitz, and H.R. Bode. 2004. HyBMP5-8b, a BMP5-8 orthologue, acts during axial patterning and tentacle formation in hydra. *Dev. Biol.* 267:43–59.

31. Wang, R., R.E. Steele, and E.M.S. Collins. 2020. Wnt signaling determines body axis polarity in regenerating Hydra tissue fragments. *Dev. Biol.* 467:88–94.

32. Landiech, S., M. Elias, P. Lapèze, H. Ajiyel, M. Plancke, B. González-Bermúdez, A. Laborde, F. Mesnilgrente, D. Bourrier, D. Berti, C. Montis, L. Mazenq, J. Baldo, C. Roux, M. Delarue, and P. Joseph. 2024. Parallel on-chip micropipettes enabling quantitative multiplexed characterization of vesicle mechanics and cell aggregates rheology. *APL Bioeng.* 8:026122.

33. Pietuch, A., B.R. Brückner, T. Fine, I. Mey, and A. Janshoff. 2013. Elastic properties of cells in the context of confluent cell monolayers: impact of tension and surface area regulation. *Soft Matter*. 9:11490–11502.

34. Harris, A.R., L. Peter, J. Bellis, B. Baum, A.J. Kabla, and G.T. Charras. 2012. Characterizing the mechanics of cultured cell monolayers. *Proc. Natl. Acad. Sci. U. S. A.* 109:16449–16454.

35. Vlad-Fiegen, A., A. Langerak, S. Eberth, and O. Müller. 2012. The Wnt pathway destabilizes adherens junctions and promotes cell migration via β-catenin and its target gene cyclin D1. *FEBS Open Bio*. 2:26.

36. Kim, W.K., Y. Kwon, M. Jang, M. Park, J. Kim, S. Cho, D.G. Jang, W. Bin Lee, S.H. Jung, H.J. Choi, B.S. Min, T. Il Kim, S.P. Hong, Y.K. Paik, and H. Kim. 2019. β-catenin activation down-regulates cell-cell junction-related genes and induces epithelial-to-mesenchymal transition in colorectal cancers. *Sci. Rep.* 9.

37. Tejeda-Muñoz, N., M. Morselli, Y. Moriyama, P. Sheladiya, M. Pellegrini, and E.M. De Robertis. 2022. Canonical Wnt signaling induces focal adhesion and Integrin beta-1 endocytosis. *iScience*. 25:104123.

38. Dzamba, B.J., K.R. Jakab, M. Marsden, M.A. Schwartz, and D.W. DeSimone. 2009. Cadherin adhesion, tissue tension, and noncanonical Wnt signaling regulate fibronectin matrix organization. *Dev. Cell*. 16:421–432.

39. Mongera, A., P. Rowghanian, H.J. Gustafson, E. Shelton, D.A. Kealhofer, E.K. Carn, F. Serwane, A.A. Lucio, J. Giammona, and O. Campàs. 2018. A fluid-to-solid jamming transition underlies vertebrate body axis elongation. *Nature*. 561:401–405.

40. Vuong-Brender, T.T.K., M. Ben Amar, J. Pontabry, and M. Labouesse. 2017. The interplay of stiffness and force anisotropies drives embryo elongation. *Elife*. 6.

41. Wang, X., M. Merkel, L.B. Sutter, G. Erdemci-Tandogan, M.L. Manning, and K.E. Kasza. 2020. Anisotropy links cell shapes to tissue flow during convergent extension. *Proc. Natl. Acad. Sci. U. S. A.* 117:13541–13551.

42. Chan, C.J., M. Costanzo, T. Ruiz-Herrero, G. Mönke, R.J. Petrie, M. Bergert, A. Diz-Muñoz, L. Mahadevan, and T. Hiiragi. 2019. Hydraulic control of mammalian embryo size and cell fate. *Nat. 2019 5717763*. 571:112–116.

43. Ruiz-Herrero, T., K. Alessandri, B. V. Gurchenkov, P. Nassoy, and L. Mahadevan. 2017. Organ size control via hydraulically gated oscillations. *Development*. 144:4422–4427.

44. Shibamoto, S., K. Higano, R. Takada, F. Ito, M. Takeichi, and S. Takada. 1998. Cytoskeletal reorganization by soluble Wnt-3a protein signalling. *Genes Cells*. 3:659–670.

45. Schreck, C., R. Istvánffy, C. Ziegenhain, T. Sippenauer, F. Ruf, L. Henkel, F. Gärtner, B. Vieth, M.C. Florian, N. Mende, A. Taubenberger, Á. Prendergast, A. Wagner, C. Pagel, S. Grziwok, K.S. Götze, J. Guck, D.C. Dean, S. Massberg, M. Essers, C. Waskow, H. Geiger, M. Schiemann, C. Peschel, W. Enard, and R.A.J. Oostendorp. 2017. Niche WNT5A regulates the actin cytoskeleton during regeneration of hematopoietic stem cells. *J. Exp. Med.* 214:165–181.

46. Bailles, A., G. Serafini, H. Andreas, C. Zechner, C.D. Modes, and P. Tomancak. 2025. Anisotropic stretch biases the self-organization of actin fibers in multicellular Hydra aggregates. *Proc. Natl. Acad. Sci.* 122:e2423437122.

Supplementary figures

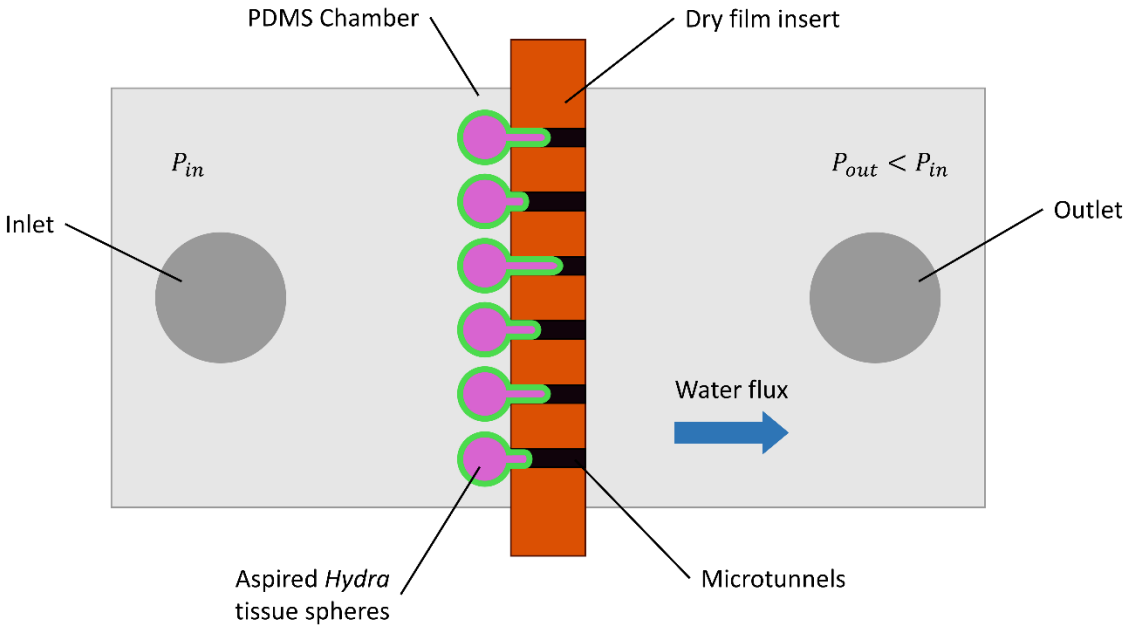

Supplementary figure 1. Schematics of the parallelized micro-aspiration setup. A PDMS channel is barred by a dry film insert pierced with six cylindrical holes. A pressure difference is applied between the inlet and outlet through hydrostatic pressure. As a result, the tissue spheres (shown in green and magenta) are aspirated within the holes.

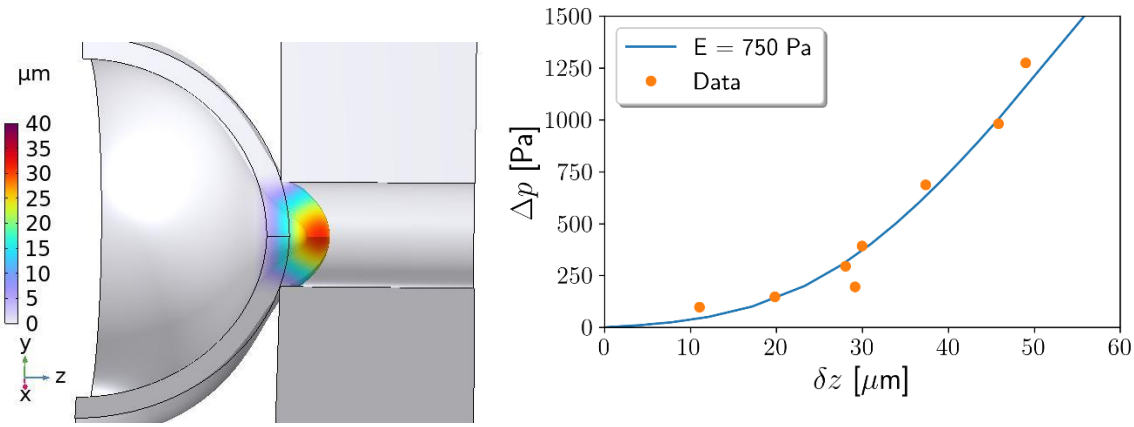

Supplementary figure 2. Numerical simulations of low applied pressure regime. Left: snapshot of the finite element simulation. The color code represents the aspirated length. It is measured as a displacement fieldfrom the reference state of the spherical shell which is shown as black lines. Right: the blue line shows a stress-strain curve obtained from a simulation with E=750Pa. This value was adjusted by trial and error to match experimental measurements on a single, control sample, shown as orange dots.

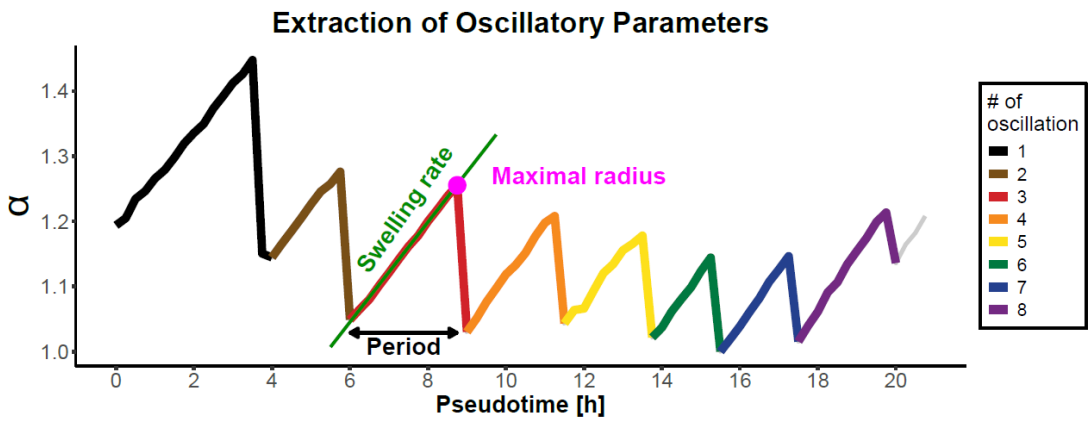

Supplementary figure 3. Schematics of measured parameters for osmotic oscillations. Each oscillation, here with a total of 8, is shown in a different color.

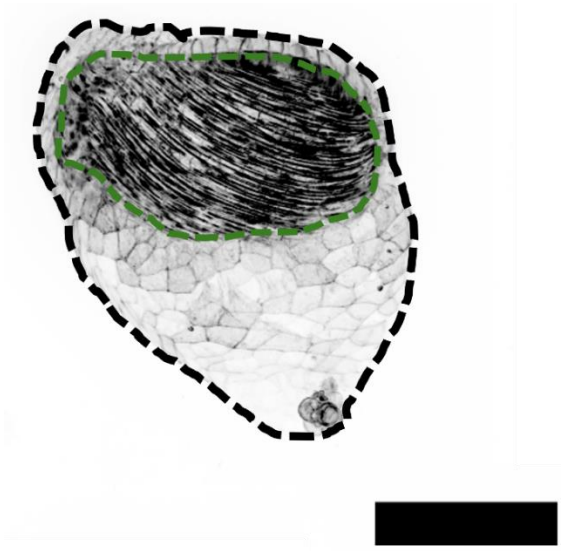

Supplementary figure 4. Schematics of the quantification of the surface covered by myonemes. The raw image shows, in black, the maximum intensity projection of the fluorescence signal from a LifeAct-GFP tissue sphere. The dashed black line is the outline of the entire sample while the green dashed line is the outline of the area covered by visible myonemes. We measured the ratio of area of these two regions and classified this sample in the 10-50% category. Scale bar: 200 microns.

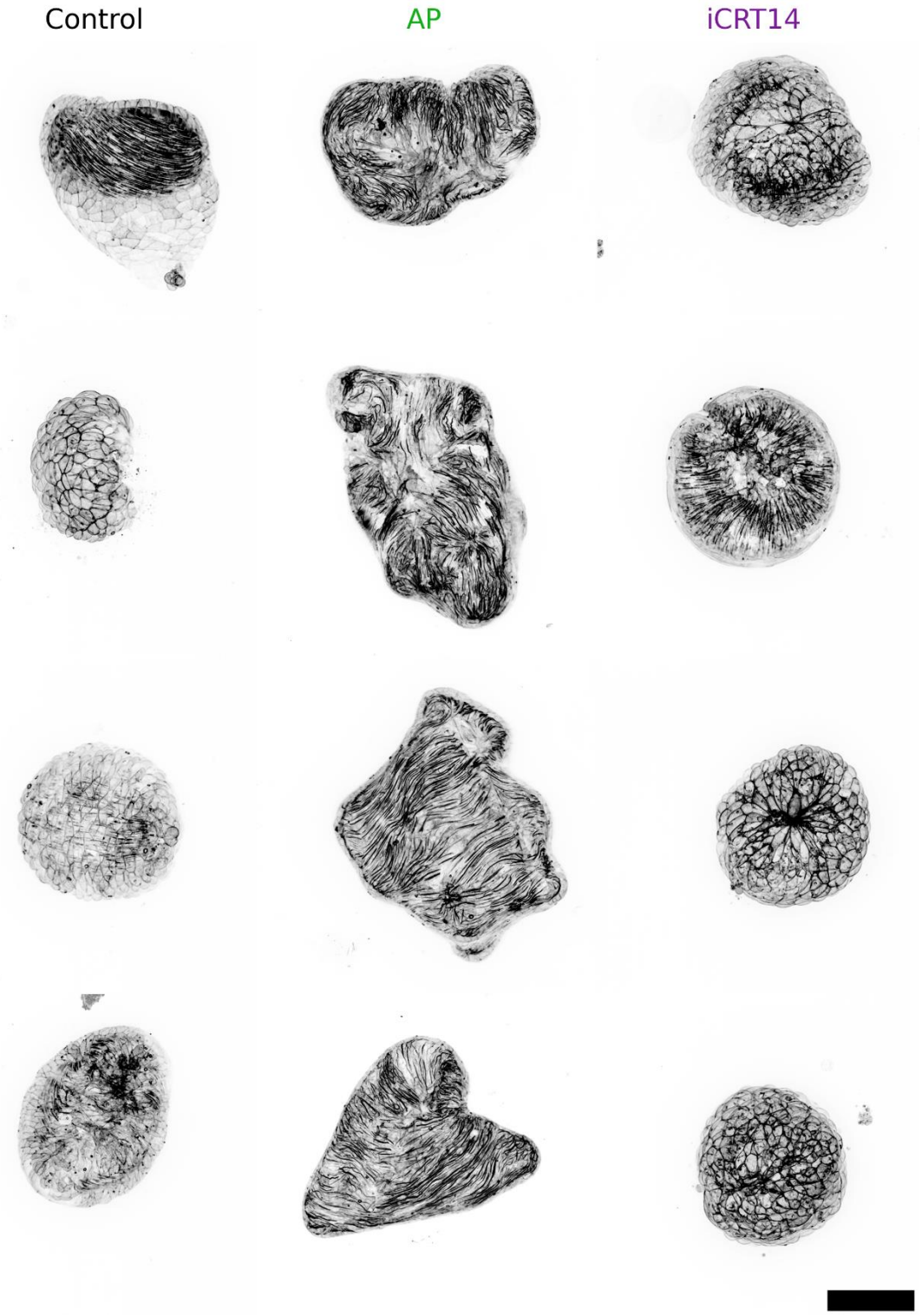

Supplementary figure 5. Maximum intensity projections of LifeAct-GFP Hydra tissue pieces in each condition (each column). Scale bar: 200 microns.

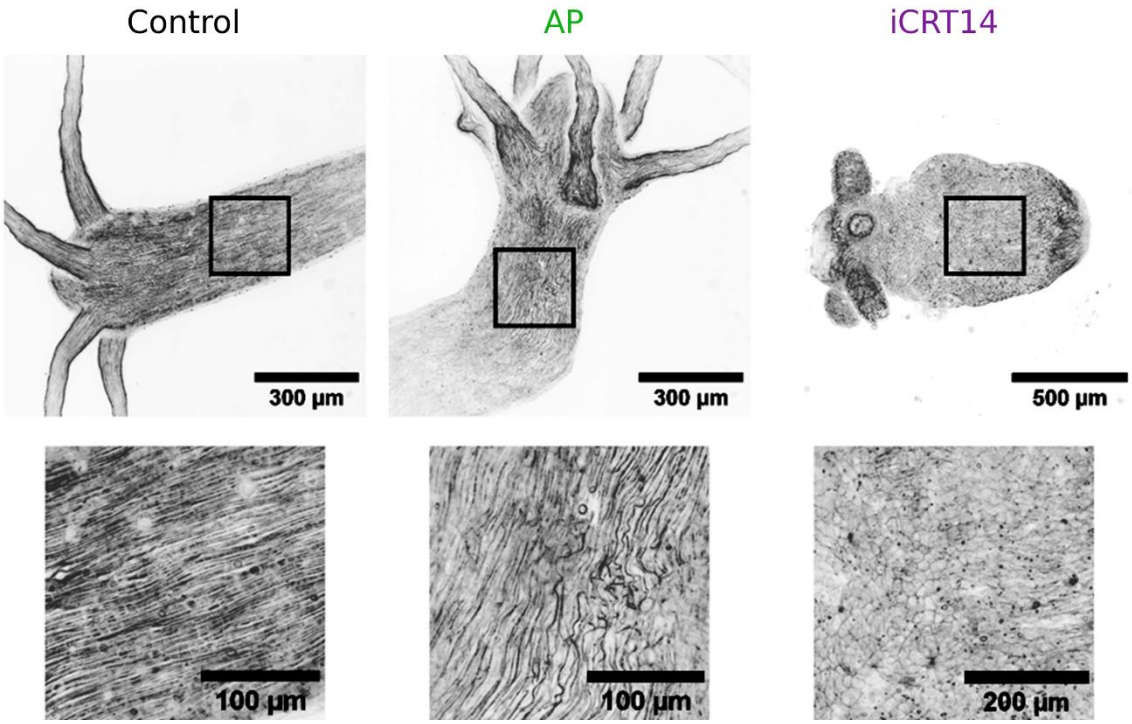

Supplementary figure 6. Maximum intensity projections of LifeAct-GFP full Hydra in each condition. The bottom row shows close ups of the regions delimited above by the black squares. Note the disorganization of myonemes under AP treatment and their local disappearance under iCRT14.